ON THE PUZZLING HIGH-ENERGY PULSATIONS OF THE ENERGETIC
RADIO-QUIET γ-RAY PULSAR J1813−1246

M. MARELLI[1], A. HARDING[2], D. PIZZOCARO[1,3], A. DE LUCA[1,4], K. S. WOOD[5], P. CARAVEO[1,4],
D. SALVETTI[1], P. M. SAZ PARKINSON[6,7], AND F. ACERO[8]

[1] INAF-Istituto di Astrofisica Spaziale e Fisica Cosmica Milano, via E. Bassini 15, I-20133 Milano, Italy; marelli@lambrate.inaf.it
[2] Astrophysics Science Division, NASA/Goddard Space Flight Center, Greenbelt, MD 20771, USA
[3] Universitá degli Studi dell'Insubria, Via Ravasi 2, I-21100 Varese, Italy
[4] Istituto Nazionale di Fisica Nucleare, Sezione di Pavia, via Bassi 6, I-27100 Pavia, Italy
[5] Space Science Division, Naval Research Laboratory, Washington, DC 20375, USA
[6] Department of Physics, The University of Hong Kong, Pokfulam Road, Hong Kong
[7] Santa Cruz Institute for Particle Physics, University of California, Santa Cruz, CA 95064, USA
[8] Laboratoire AIM, CEA-IRFU/CNRS/Universit Paris Diderot, Service d'Astrophysique, CEA Saclay, F-91191 Gif sur Yvette, France

ABSTRACT

We have analyzed the new deep *XMM-Newton* and *Chandra* observations of the energetic, radio-quiet pulsar J1813−1246. The X-ray spectrum is nonthermal, very hard, and absorbed. Based on spectral considerations, we propose that J1813 is located at a distance further than 2.5 kpc. J1813 is highly pulsed in the X-ray domain, with a light curve characterized by two sharp, asymmetrical peaks, separated by 0.5 in phase. We detected no significant X-ray spectral changes during the pulsar phase. We extended the available *Fermi* ephemeris to five years. We found two glitches. The γ-ray light curve is characterized by two peaks, separated by 0.5 in phase, with a bridge in between and no off-pulse emission. The spectrum shows clear evolution in phase, being softer at the peaks and hardening toward the bridge. Surprisingly, both X-ray peaks lag behind the γ-ray ones by a quarter of phase. We found a hint of detection in the 30–500 keV band with *INTEGRAL*, which is consistent with the extrapolation of both the soft X-ray and γ-ray emission of J1813. The unique X-ray and γ-ray phasing suggests a singular emission geometry. We discuss some possibilities within the current pulsar emission models. Finally, we develop an alternative geometrical model where the X-ray emission comes from polar cap pair cascades.

Key words: gamma rays: stars – pulsars: general – pulsars: individual (PSR J1813−1246) – stars: neutron –
X-rays: stars

Online-only material: color figures

1. INTRODUCTION

The Large Area Telescope (LAT) on board the *Fermi Gamma-ray Space Telescope* (hereafter *Fermi*-LAT) is providing new insights into the γ-ray pulsar population, revolutionizing our understanding of pulsar high-energy emission (Caraveo 2014). The wealth of detections (Abdo et al. 2013) confirms the importance of the γ-ray channel in the overall energy budget of rotation-powered pulsars and paves the way for a better understanding of the three-dimensional structure and electrodynamics of neutron star magnetospheres. Indeed, radio and γ-ray light curves are shaped by the geometry as well as by the emission processes at work in pulsar magnetospheres (see, e.g., Watters & Romani 2011; Pierbattista et al. 2012, 2014). Based on the phenomenology of $\sim$150 γ-ray detections, models with emission originating at high altitudes in the magnetosphere (e.g., outer and slot-gap; Cheng et al. 1986; Harding & Muslimov 2004) are favored over models with near-surface emission (e.g., polar cap; Harding 2013).

Fitting γ-ray and radio light curves simultaneously is a promising way to constrain geometric parameters of the pulsar (e.g., Pierbattista et al. 2014). Exploiting the (magnetospheric) nonthermal pulsar X-ray light curves could further improve such an approach, adding another piece to the pulsar emission puzzle. This would also allow the localization of the emitting region(s) responsible for the nonthermal pulsed X-ray emission with respect to the high altitude γ-ray emitting one(s).

Pulsar X-ray light curves are very diverse, with one or more peaks, broad or narrow, and a range of phase lags between radio, γ-ray, and X-ray peaks. Indeed, with the notable exception of the Crab pulsar (among the young ones), the multi-wavelength behavior of isolated neutron stars is complex, with radio, optical, X-ray, and γ-ray light curves usually misaligned, pointing to different, and currently unknown, emitting regions in the pulsar magnetosphere. The rich X-ray phenomenology has not yet been fully exploited, leaving a number of open questions.

Here we report the results of deep joint *XMM-Newton* and *Chandra* observations aimed at searching for pulsations and performing a phase-resolved spectral analysis of the radio-quiet *Fermi*-LAT pulsar J1813−1246 (hereafter J1813) in the soft X-ray band (0.3–10 keV). Our X-ray observations also enable us to study the possible extended emission from its pulsar wind nebula (PWN).

J1813 was discovered within a few months of the launch of *Fermi*, in a blind pulsation search of LAT data (Abdo et al. 2009a). It is one of the brightest γ-ray pulsars, making it into the *Fermi*-LAT Bright Source List as 0FGL J1813.5−1248 (Abdo et al. 2009b). Its period $P \sim 48.1$ ms and period derivative $\dot{P} \sim 1.76 \times 10^{-14}$ s s^{-1} point to a spin-down energy-loss rate $\dot{E} \sim 6.24 \times 10^{36}$ erg s^{-1} and a characteristic age $\tau_c = 43$ kyr, making it the fastest-spinning known radio-quiet pulsar and the second most energetic one (see Abdo et al. 2013). Its γ-ray light curve exhibits two fairly broad peaks 180° apart (peak phase separation of 0.49 ± 0.01), with a clear asymmetric

bridge emission (Abdo et al. 2013). Although there is no reliable distance measurement for J1813, its pseudo-distance, which hinges on the observed correlation between intrinsic γ-ray luminosity and $\dot{E}$ (Saz Parkinson et al. 2010), is $\sim$1.5 kpc (this would result in a γ-ray efficiency of $\sim$0.01, typical of energetic γ-ray pulsars). This pulsar exhibited a glitch around 2009 September 20 (Ray et al. 2011). Despite dedicated Green Bank Telescope radio observations at 0.82 and 2 GHz, no radio emission was detected down to a 17 μJy limit (Abdo et al. 2013). A possible X-ray counterpart was detected by *Swift* soon after the discovery of the pulsar (Abdo et al. 2009a), and was confirmed to be coincident with the precise *Fermi*-LAT timing position (Ray et al. 2011). The bright (10^{-12} erg cm^{-2} s^{-1}) X-ray counterpart unveiled by *Swift* (Marelli et al. 2011) was later confirmed by *Suzaku* (Abdo et al. 2013), and possibly associated with a nebular emission extending up to a few tens of arcseconds.

2. OBSERVATIONS AND DATA REDUCTION

Our deep *XMM-Newton* observation of J1813 was performed on 2013 March 10 and lasted 108.9 ks. The PN camera (Struder et al. 2001) of the EPIC instrument was operating in Small Window mode, with a time resolution of 5.6 ms over a $4' \times 4'$ field of view (FOV), while the metal oxide semi-conductor (MOS) detectors (Turner et al. 2001) were set in Full Frame mode (2.6 s time resolution on a $15'$ radius FOV). The thin optical filter was used for the PN and the medium filter for the MOS cameras. We used the *XMM-Newton* Science Analysis Software (SAS) v13.0. We performed a standard analysis of high particle background (following De Luca et al. 2005). We cross-checked the results with the SAS tool `bkgoptrate` (also used for the 3XMM source catalog[8]). This tool searches for the point at which the maximum signal-to-noise (S/N) ratio is achieved for the given background time series after the bins above a threshold are excluded. Both analyses revealed no significant contamination from flares. We selected 0–4 pattern events for PN and 0–12 for the MOS detectors in the 0.3–10 keV energy range, following Marelli et al. (2013). Then, we excluded the 0.3–0.4 keV energy range for the PN owing to the presence of bright columns. Due to the high degree of absorption in our source, the number of expected counts in the 0.3–0.4 keV energy range is negligible (10^{-12} counts s^{-1} for the best fit spectrum, obtained using the WebPimms HEASARC tool). For each spectrum we generated ad hoc response matrices and effective area files using the SAS tools `rmfgen` and `arfgen`.

To fully characterize both the pulsar and its putative nebula, we also obtained a *Chandra*/ACIS-S (Garmire et al. 2003) exposure of the field. The observation was performed on 2013 July 22 and lasted 50.4 ks. The telemetry mode was set to Very Faint, which was recommended to reduce background in extended sources. We used the *Chandra* Interactive Analysis of Observation (CIAO) software v4.5. We also re-analyzed a public 25.7 ks *Suzaku* (Mitsuda et al. 2007) observation performed on 2010 March 22. The HEAsoft package (v6.15) was used to analyze *Suzaku* data, following the standard recommendations.[9]

3. γ-RAY ANALYSIS

The *Fermi*-LAT data set we used to extend the γ-ray ephemeris of J1813 spans five years, from 2008 August 4 to 2013 August 4. P7REP `Source` class events were selected with reconstructed energies from 0.1 to 100 GeV and with arrival directions within $20°$ of the source position. We excluded γ-rays collected when the LAT was not in nominal science operations mode, when the spacecraft rocking angle exceeded $52°$, or when the Sun was within $5°$ of the pulsar position. Moreover, to reduce contamination by residual γ rays from the bright limb of the Earth, we excluded photons with measured zenith angles $>100°$. We performed a binned maximum likelihood analysis, following Abdo et al. (2013). We used the *Fermi* Science tools v09r32p04, Instrument Response Functions P7REP_SOURCE_V15, the Galactic and isotropic models obtained by the LAT collaboration from the analysis of four years of data.[10] The analysis tools, instrument response functions, and diffuse emission models are available from the *Fermi* Science Support Center.[11] The source models were taken from the two-year source and pulsar catalogs (Nolan et al. 2012; Abdo et al. 2013). In our model of the region, post-fit spatial residuals did not reveal the need for any additional source beyond those in the two-year catalog. The pulsar γ-ray spectrum is consistent with a power law with an exponential cutoff with $\Gamma = 2.15 \pm 0.02$ and cutoff energy $E_c = 3.6 \pm 0.3$ GeV (1σ errors). These results are in agreement with those in Abdo et al. (2013).

Since Kerr (2011) reports an increase in the sensitivity to pulsations by more than 50%, under a wide range of conditions, when using photon weighting techniques on *Fermi*-LAT sources, we used the *Fermi* Science Tool `gtsrcprob`, which combines the spectral results with the energy-dependent point-spread function (PSF) of the LAT to assign to each event its probability of coming from the pulsar (Kerr 2011). For our timing analysis we used only barycentered events with a probability greater than 0.01. The rotational ephemeris used in Abdo et al. (2013) spans only three years: we extended it, using a weighted Markov Chain Monte Carlo algorithm (MCMC; see, e.g., Wang et al. 2013). Adding six months of data in each iteration, we re-evaluated the timing solution using the *H* test (see e.g., De Jager & Busching 2010). Apart from the glitch reported in Ray et al. (2011), we detected a second one (at MJD = 56290; see Table 1). By separately analyzing the three time intervals (before the first glitch, between the two, and after the last one) we obtained the best ephemeris and light curve for each period. Then, following Abdo et al. (2013), we fitted each curve with a composite model encompassing a constant and three Gaussians. Using the relative positions of each Gaussian maximum, we extracted the relative phases of the three light curves and built the five-year J1813 ephemeris reported in Table 1.

Using our ephemeris, we assigned a rotational phase to each γ-ray event and filled a 100 bin >0.1 GeV phase histogram, with bin uncertainties taking into account the photon weights (see Figure 1). J1813 being a radio-quiet pulsar, phase 0 was chosen arbitrarily at $\mathrm{MJD}_0 = 56362.0$. Our light curve is consistent with the one from Abdo et al. (2013) and is characterized by two peaks: the maximum of the first peak is at phase 0.258 ± 0.003 and the second at phase 0.743 ± 0.002. The separation between the peaks is 0.485 ± 0.003 in phase, with a bridge of emission between the peaks. While the normalization of the two peaks is similar, the first one is asymmetric with a clear trail. Following the prescriptions of Abdo et al. (2013), we obtained an acceptable fit ($\chi^2_{\mathrm{red}} = 1.78$, 40 dof, null hypothesis probability,
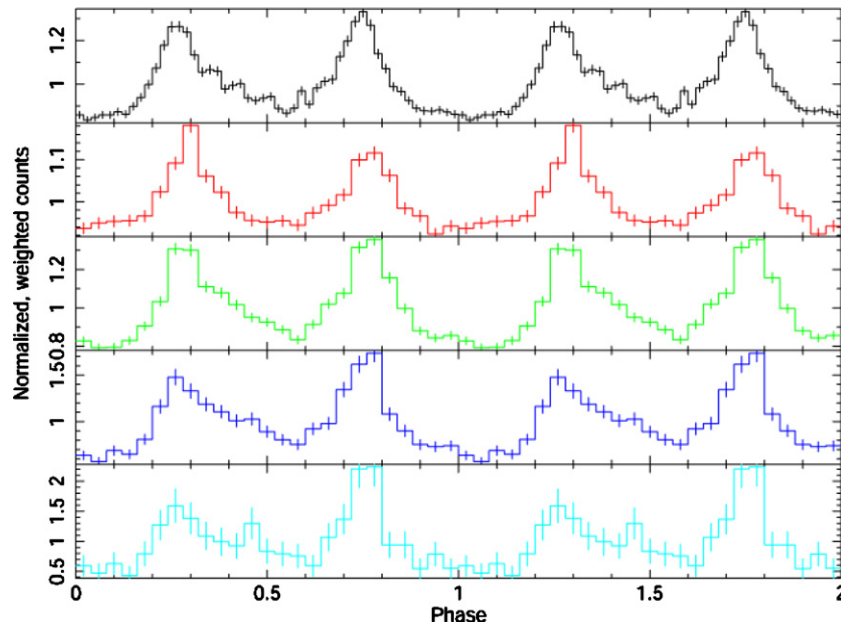
Figure 1. Normalized, weighted *Fermi* γ-ray light curves, using the ephemeris described in Section 3 and with MJD$_0$ = 56362.0. From the top panel, the curves are in the >0.1 GeV, 0.1–0.3 GeV, 0.3–1 GeV, 1–3 GeV, and >3 GeV energy ranges, respectively. The curves have been renormalized by dividing each bin by N_{counts}/N_{bins}, where N_{counts} is the total weighted number of events in the energy range and N_{bins} the number of bins. 1σ errors are shown.

(A color version of this figure is available in the online journal.)

Table 1
J1813 Ephemeris

Validity Period MJD	F0 (Hz)	F1 (10^{-12} Hz^2)	F2 (10^{-22} Hz^3)	F3 (10^{-30} Hz^4)	F4 (10^{-37} Hz^5)	F5 (10^{-44} Hz^6)	H-value ⋯	ΔPhase[a] ⋯
54682–55114	20.80104237955	−7.93199	−78.201	−121.557	−9.347	0	720	⋯
55114–56290	20.80107402437	−7.63091	−7.966	−52.707	−20.321	−3.85	1617	−0.037 ± 0.005
56290–56508	20.80107410361	−7.62139	−6.1725	−1.753	0	0	235	0.345 ± 0.007

Notes. Ephemeris of J1813 at MJD$_0$ = 56362.0, corresponding to the X-ray observation epoch. High-level derivatives have been added in order to improve the *H*-value (20 harmonics), so that they are not related to physical values. The *H*-values obtained are proportional to the number of photons considered (∝ validity period).
[a] ΔPhase = Phase$_{fin}$−Phase$_{in}$ is evaluated using the phase lag between the two maxima; a positive value implies a shift of the peaks toward right in the light curve.

nhp = 0.002) using two Gaussians to describe the first peak and one for the second.[12]

To perform a >0.1 GeV γ-ray phase-resolved spectral analysis on the 5-year data set, we rebinned the light curve into 25 bins. For each phase bin, we re-ran the binned likelihood spectral analysis to search for variations in the spectral parameters as a function of the pulsar phase. We used the same region of the phase-averaged analysis, but we fixed spectral parameters of all the other sources at the best fitted ones. We left free to vary all the spectral parameters of J1813, as well as the Galactic and isotropic spectral parameters. Anyway, we note that we obtain consistent results by freezing the Galactic and isotropic spectral parameters. A simple χ^2 to test the variation of the best fitted parameters, leaving all the pulsar spectral parameters free to vary, is not adequate since such parameters are correlated and a single parameter variation cannot describe the overall spectral change. To search for spectral variation, we can compare the best fit test statistic (TS) of models with one or more parameters left free to vary in each bin. While a source TS is usually used

to gauge the source significance against a model that does not contain such source (model 0) (Mattox at al. 1996; Cash 1979), we can build a TS that expresses the likelihood ratio between the source spectral model with a parameter fixed (model 1) and the same model with the same parameter left free (model 2) by using

$$\mathrm{TS}_{2vs1} = -2\ln\frac{L_1}{L_2} = -2\ln\frac{L_0}{L_2} + 2\ln\frac{L_0}{L_1} = \mathrm{TS}_{2vs0} - \mathrm{TS}_{1vs0}. \quad (1)$$

For high statistics, such TS follows a distribution similar to a χ^2 with one degree of freedom. All the boundary conditions, as defined in Cash (1979) and Protassov et al. (2002), are verified in this case. For a phase-resolved spectral analysis, we are considering N (in our case 25) bins. In such a case, we can obtain a $\mathrm{TS}_{2vs1,tot}$ which expresses the probability that a given parameter is constant during the phase as

$$\mathrm{TS}_{2vs1,tot} = -2\ln\prod_{i=1}^{N}\left(\frac{L_1}{L_2}\right)_i = \sum_{i=1}^{N}\left(-2\ln\frac{L_{0,i}}{L_{2,i}} + 2\ln\frac{L_{0,i}}{L_{1,i}}\right)$$

$$= \sum_{i=1}^{N}(\mathrm{TS}_{2vs0,i} - \mathrm{TS}_{1vs0,i}). \quad (2)$$

---

[12] The nhp is the probability of obtaining a test statistic result at least as extreme as the one that was actually observed, assuming that the null hypothesis is true.
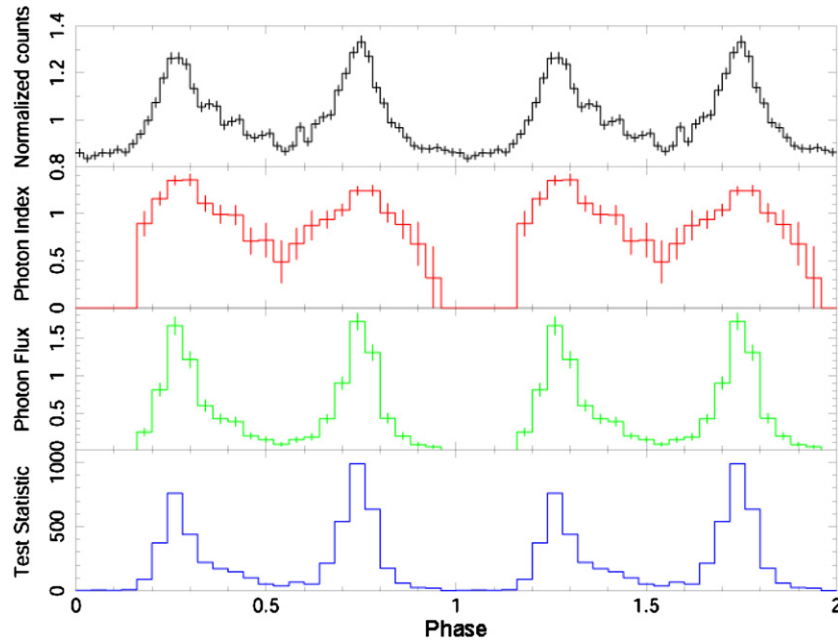
Figure 2. Results of *Fermi* phase-resolved spectroscopy leaving free to vary only normalization and photon index. Black: >0.1 GeV normalized, weighted light curve; red: best fitted photon indexes (only for bins with TS > 25); green: best fitted photon fluxes (10^{-8} photons cm^{-2} s^{-1}); blue: test statistic of the fits. 1σ errors are shown.

(A color version of this figure is available in the online journal.)

For high statistics, such TS follows a distribution similar to a χ^2 with N degrees of freedom. Applying this to our phase-resolved spectroscopy, the TS of variable normalization+index and variable normalization+cutoff, both compared to the only-normalization variation, are $TS_{2vs1,tot} = 1780$ and $TS_{2vs1,tot} = 624$, respectively. We can therefore conclude that there is a spectral variation of J1813 with phase. The change of the photon index is much more compelling than the variation in the cutoff energy. As is apparent in Figure 2, the spectrum softens during each peak, while it is harder during the bridge between the two peaks.

At variance with the finding of Abdo et al. (2013), our five-year light curve does not show a significant off-pulse emission. As an off-pulse interval we chose the bins in which the source has TS < 25 both in each bin and in the entire interval. Indeed, when selecting the phase interval 0.96–0.16, the source is barely detected at the $\sim$3σ level. We note that due to the improvement in the statistics and models, the off-pulse interval we use is shorter than that in 2PC. Improved models of diffuse Galactic and isotropic background emission are probably responsible for this result.

4. X-RAY OBSERVATIONS AND ANALYSIS

Figure 3 shows the 0.3–10 keV *XMM-Newton* FOV. Source detection using maximum likelihood fitting was done simultaneously on each of the EPIC-PN, MOS1, and MOS2 with the SAS tool `edetect_chain`. We also performed a source detection on the *Chandra* data set by using the CIAO tool `wavdetect`.

The best X-ray position of the pulsar is $18^h13^m23^s.77$, $-12°45'59''.9$ ($0''.015 + 0''.6$ 90% statistical plus systematic errors). We analyzed the pulsar radial brightness profiles in *XMM-Newton* and *Chandra* data sets and compared them with the theoretical PSFs. The PSF of the EPIC-PN camera on board *XMM-Newton* is best described by an off-axis, energy-dependent King function (Read 2004). The FWHM of the PSF

for an on-axis source at 1.5 keV is typically less than $12''.5$ for the PN camera and $4''.4$ for the two MOS detectors.[13] The theoretical *Chandra* PSF is much more complicated and is largely off-axis-dependent; its evaluation requires simulations of the specific observation using `Chart` and `MARX`. The observed PSFs, the fit with the *XMM-Newton* theoretical one, and the *Chandra* PSF simulation for a point-like source are shown in Figure 4. The observed *XMM-Newton* brightness profile is well fitted by the theoretical PSF ($\chi^2_{red} = 1.1$, dof = 5, nhp = 0.39) and the observed and simulated *Chandra* profiles agree (fitting the residuals with a constant, we obtain $\chi^2_{red} = 2.4$, dof = 15, nhp = 0.01). We therefore conclude that no extended emission is detected down to a fraction of an arcsecond. The *Suzaku* detection of a nebula, reported in Abdo et al. (2013), is due to source #7, located $50''$ from the pulsar.

Figure 3 shows the brightest sources in the PN FOV. The study of the line-of-sight absorption of such sources could allow us to constrain the pulsar distance. Indeed, after selecting candidate active galactic nuclei (AGNs) in the FOV, it is possible to measure from their spectra the total Galactic column density in the direction of J1813. Next, using the pulsar column density, we can get an estimate of its distance with respect to the edge of the Galaxy. Such estimate could be refined if bright X-ray and optical stars (with known distance) were also present (see, e.g., Marelli et al. 2013, 2014).

Based on the study of spectra and possible optical counterparts, we classified serendipitous sources as AGNs or candidate stars (see the Appendix). Our exercise allowed us to identify four very likely AGNs and three stars.

The spectra of the AGNs show very high values of column density ($(1–2) \times 10^{22}$ cm^{-2}), higher than the value of 7×10^{21} cm^{-2} obtained from the 21 cm H I sky survey of Kalberla et al. (2005). Given the unexpectedly high values of column

---

[13] http://xmm.esac.esa.int/external/xmm_user_support/documentation/sas_usg/USG/
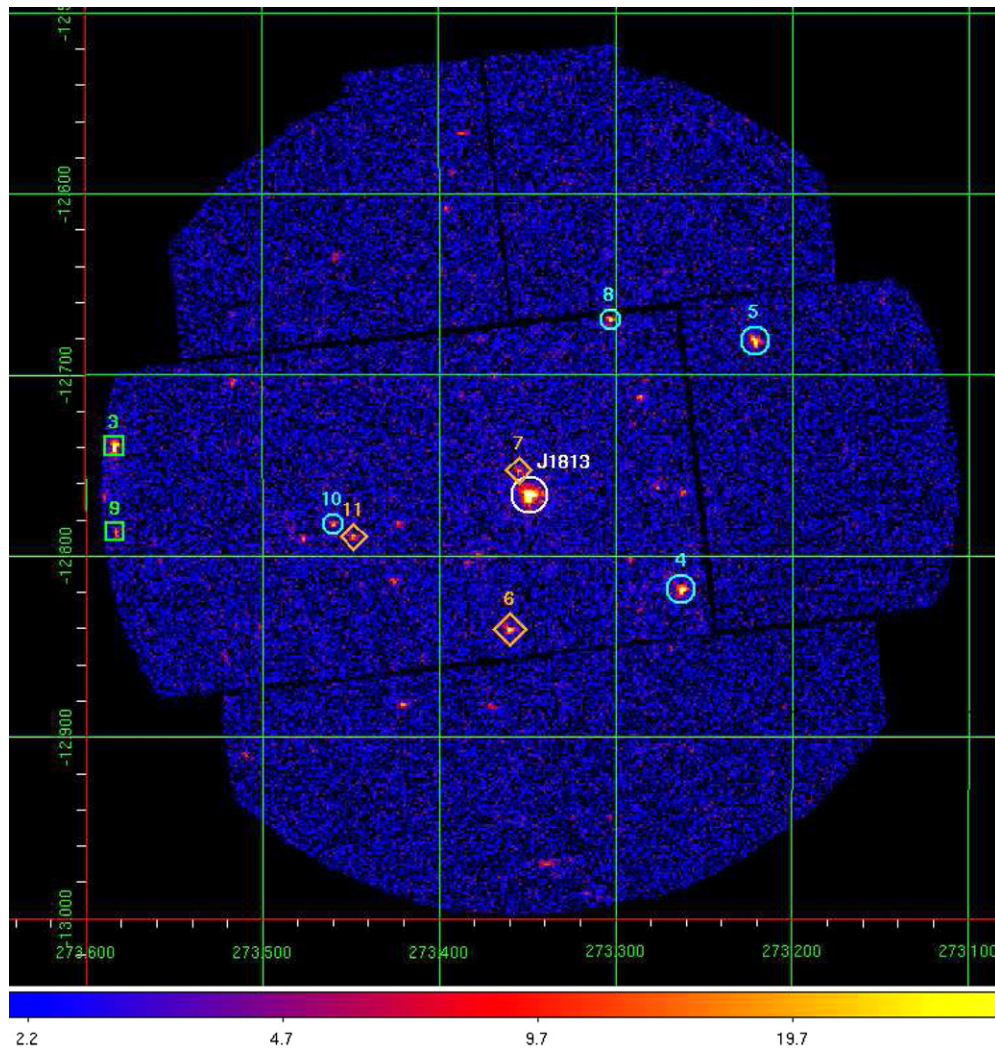
Figure 3. 0.3–10 keV field of view of *XMM-Newton* MOS2 camera. The pulsar is circled in white, the X-ray emitting stars in orange, the AGNs in cyan, and the unidentified sources in green.
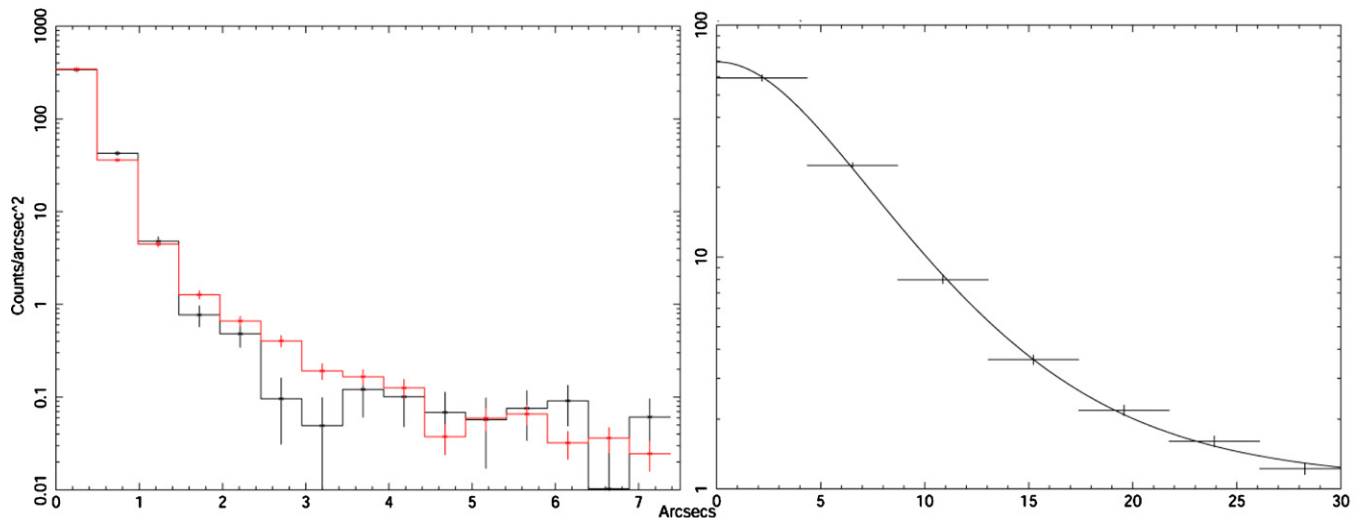
Figure 4. Left: the *Chandra* radial brightness profile of J1813 (black) and the simulated one (red). Right: the *XMM-Newton* radial brightness profile of J1813 and its best fit with a constant plus King function. Both fits point to a lack of diffuse emission down to fractions of arcsec.

density of the sources inside the *XMM-Newton* FOV, we searched for the presence of molecular clouds in that region. The all-sky model of dust emission from *Planck* (Abergel et al. 2014) allows us to estimate the dust temperature uniformly over the entire sky, providing an improved estimate of the dust optical depth compared to previous all-sky dust model. The region of J1813 is characterized by a higher temperature than the mean of that latitude, pointing to a higher absorption than usual. Dobashi
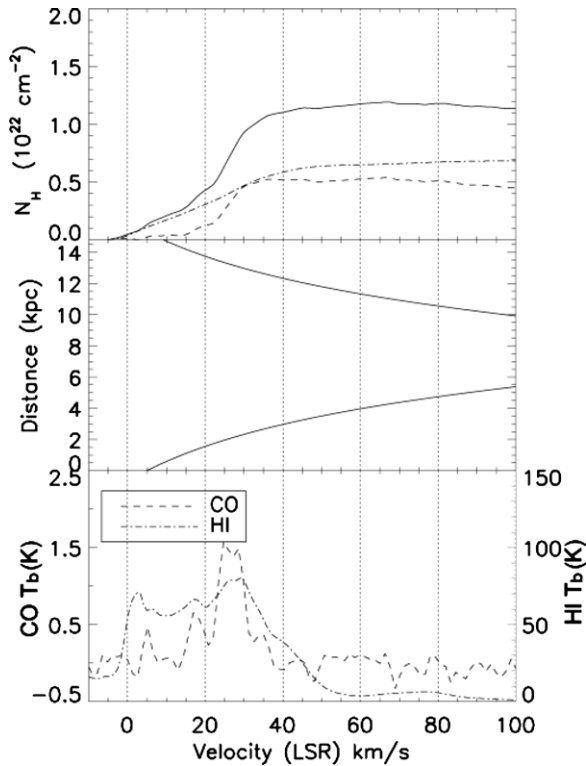
Figure 5. Top: cumulative absorption column N_H (solid line) toward J1813 derived from atomic (H I, dotted line) and molecular (^{12}CO, dashed line) gas. Middle: distance as a function of radial velocity derived from the Galactic rotation curve model of Hou et al. (2009). Bottom: ^{12}CO (dashed line) and H I (dotted line) spectra at the position of the pulsar.

(2011) presents an atlas and catalog of dark clouds derived from the Two Micron All Sky Survey Point Source Catalog (2MASS PSC; Skrutskie et al. 2006) and reports four dark clouds within the *XMM-Newton* FOV, with a structured pattern. The discrepancy between the Galactic absorption and the N_H values of our AGN-like sources should be ascribed to the presence of such an irregular pattern of dark clouds.

The best-fit N_H value of J1813 will indicate if the pulsar is located in front or in the rear of those clouds. With the distance to the clouds known, this will become an important estimator of the pulsar distance.

In fact, a comparison of the X-ray absorption column along the line of sight obtained with the column density derived from the atomic (H I) and molecular (^{12}CO, $J = 1 \rightarrow 0$ transition line) gas can be used to provide a lower limit on the distance of J1813. The data from the ^{12}CO Dame et al. (2001) CfA survey and from the H I Parkes Galactic all-sky survey (McClure et al. 2009; Kalberla et al. 2005) are used. The CO-to-H$_2$ mass conversion factor used is 1.8×10^{20} cm^{-2} K^{-1} km^{-1} s (Dame et al. 2001) and the H I brightness temperature to column density is 1.82×10^{18} cm^{-2} K^{-1} km^{-1} s (Dickey & Lockman 1990). The Galactic rotation curve model of Hou et al. (2009) is used to translate the measured velocities into distances. All absorbing material is assumed to be at the near distance allowed by the Galactic rotation curve. As shown in Figure 5, the main ^{12}CO absorption feature along the line of sight is located at a radial velocity relative to the local standard of rest (LSR) of $V_{\rm LSR} = 27$ km s^{-1} corresponding to an integrated column density of 1×10^{22} cm^{-2} (HI+^{12}CO). Therefore, if the fitted X-ray column density of J1813 is higher than this value (see the

next section), we conclude that the pulsar is located behind the clouds at a distance >2.5 kpc.

4.1. X-Ray Spectral Analysis

To study the spectrum of J1813, we simultaneously fitted spectra from *XMM-Newton*, *Chandra*, and *Suzaku*. For *XMM-Newton*, we chose an extraction radius of 25″ in order to avoid contamination from the bright source located at 50″. We obtained 6072, 2581, and 2757 net counts in the 0.4–10 keV energy range in the PN and the two MOS detectors, respectively, taking into account the background contribution (9%, 4%, and 4%, respectively). For *Chandra* we chose an extraction radius of 2″ and we obtained 1494 net counts in the 0.3–10 keV energy range, taking into account the background contribution (less than 0.1%). For *Suzaku*, we chose an extraction radius of 70″ to minimize the contamination from the nearby source. With the chosen extraction radius, such a contamination is expected to be negligible ($\sim$1.5% of the total counts). From *Suzaku*, we obtained 403, 318, and 435 net counts in XIS 0, 1, and 3, respectively, taking into account the background contribution (16%, 37%, and 13%, respectively).

The very hard spectrum of J1813 is well fitted ($\chi^2_{\rm red} = 1.09$, null hypothesis probability = 0.08) by a power law with $\Gamma = 0.85 \pm 0.03$, absorbed by a column density $N_H = 1.56 \pm 0.07 \times 10^{22}$ cm^{-2} (1σ confidence level). A composite thermal plus non-thermal model is not statistically needed. In fact, an *F* test (Bevington 1969) shows that the probability for a chance improvement by using the composite spectral model is 0.003, less than a 3σ significance level. The unabsorbed 0.3–10 keV flux of J1813 is $1.08 \pm 0.01 \times 10^{-12}$ erg cm^{-2} s^{-1}, leading to a γ-ray-to-X-ray flux ratio of 234 ± 6, three times less than the lowest one of the radio-quiet pulsar family (Marelli et al. 2011; Abdo et al. 2013). Such a low value of the γ-ray-to-X-ray flux ratio is different from the higher value reported in 2PC for J1813 (1840^{+330}_{-610}). That result was based only on the short *Suzaku* and *Swift* observations, thus the low statistic prevented a correct characterization of the source. Moreover, the extracted *Suzaku* spectrum was contaminated by the nearby star (source #7 in Figure 3): such a soft spectrum prevented them from a correct evaluation of the column density, resulting in a lower value of the unabsorbed X-ray spectrum on which the γ-ray-to-X-ray flux ratio is based. We also note that in 2PC 30% of J1813 total flux was expected to come from thermal and nebular emission.

4.2. X-Ray Timing Analysis

To search for X-ray pulsations from J1813, we used the SAS tool `barycen` to barycenter the PN events using the precise *Chandra* pulsar position. In order to improve the sensitivity to pulsations, we decided to apply a photon-weighting technique similar to the one used for *Fermi*-LAT, assigning to each photon a probability of coming from the pulsar, in order to help with background rejection and improve the sensitivity to pulsations. Kerr (2011) notes that this technique is applicable to any photon-counting instrument in which sources are not perfectly separated from their background, e.g., searches for X-ray pulsation in observations of a pulsar. While in the X-ray domain, the positional errors are much smaller than in the γ-ray band, and the problem of superposition of sources is more critical. Indeed, the wide range of spectral shapes for different source classes in X-rays and the complexity of the background of X-ray telescopes (for *XMM-Newton*, see, e.g., Kunz & Snowden 2008) make such techniques as important as in the γ-ray domain.

To this end, we developed and used a Python tool to assign to each photon weights quantifying the probability that such an event comes from each of the sources within the region of interest. The tool requires the following.

(1) The position, (best fitted) spectral model, flux, and fitted PSF of each source.
(2) The (best fitted) spectral model and flux of the background.

The tool produces columns of weights that are added to the events file, replicating the *Fermi* tool `gtsrcprob`. Tests conducted on a sample of pulsars (e.g., the magnificent seven pulsars and Geminga; Treves et al. 2001; Caraveo et al. 2004) resulted in a significant improvement of the *H*-value with respect to unweighted periodicity tests with optimized spatial and energy cuts. The ratio $H_{\mathrm{weight}}/H_{\mathrm{unweight}}$ ranges from 1.2 for bright, soft sources to 2 for faint sources with hard spectra.

Similar to the γ-ray timing analysis, for J1813, we used a weighted MCMC algorithm (20 harmonics) to search for the best pulsar period during the one-day long *XMM-Newton* observation, also testing the extended *Fermi*-LAT ephemeris we found. The best frequency at MJD_0 is 20.80107408901 Hz (*H*-value = 12092, where an *H*-value of 95 yields a 5σ significance), consistent with the one from *Fermi*-LAT ephemeris (that yields *H*-value = 12088). For comparison, an unweighted test with the best energy and spatial cuts yields an *H*-value of 11123. Such best fit *H*-values have been obtained by using *XMM-Newton* events that are not randomized. In the Small Window mode of the EPIC-PN camera, arriving photons are read only during a cycle of 3.9809 ms (=integration time), then the charges are transferred (transfer time = 0.068 ms) and read (readout time = 1.521 ms). The real arrival time of each photon is then stored as a multiple of the frame time (=integration+transfer+readout time) of $\sim$5.7 ms (Kuster 1999). For standard analysis, a tool included in the SAS `epproc` usually randomizes the arrival time of each event within the 5.7 ms windows. Here, we chose not to randomize the arrival times in order to achieve a better timing resolution for our fast rotating pulsar. The un-randomized event file basically consists of sets of photons with the same arrival times at the middle of each 5.7 ms window. By using this type of event, we avoid the error from the randomization process on the entire 5.7 ms window (while the integration time is only 4 ms). For comparison, a randomized, unweighted test on J1813 with the best energy and spatial cuts gives an *H*-value of 8735.

The resulting X-ray light curve shows two very sharp peaks, about 8 ms wide, with an off-pulse component detected with a 17σ significance. Here, we define as off-pulse the sum of phase bins for which the count rate can be fitted by a constant. All the bins that deviate more than 3σ from the fitted value are considered on-pulse. In such a way, we obtain two off-pulse intervals, between 0.15–0.4 and 0.65–0.9 in phase. The pulse profile is expected to be heavily affected by the PN camera frame time binning. Thus, we developed a Python script to simulate the deformation of simple input light curves due to such PN (Small Window mode) readout cycles.

Simple input step functions cannot reproduce the measured pulse profile. A two-Gaussian model is instead able to reproduce the observed profile (see Figure 6). By using our simulation, we concluded that the X-ray pulsar profile (before the deformation due to *XMM-Newton* frame time binning) is well described by two Gaussians located at phases 0.0205 ± 0.0005 (peak1), and 0.5248 ± 0.0007 (peak2), with standard deviations of $(3.30 \pm 0.08) \times 10^{-2}$ and $(3.05 \pm 0.05) \times 10^{-2}$; the normalization of

the first peak is a factor 1.48 ± 0.05 lower than that of the second one. The separation between the first and the second peaks is 0.4957 ± 0.0009, a value in agreement (within 3σ) with the γ-ray one. Both X-ray peaks are slightly asymmetric, have tails, and their fitting requires two Gaussians, reminiscent of the first γ-ray peak. Using an *F* test, we determined that the probability for a chance improvement is 4.1×10^{-7}, pointing to a significant improvement by adding two more Gaussians. The peak of the first γ-ray Gaussian lags behind the peak of the first X-ray Gaussian by 0.237 ± 0.002 in phase and the peak of the second γ-ray Gaussian lags behind the second X-ray peak by 0.218 ± 0.003 in phase (Figure 7).

By definition, the weighted light curve is background-subtracted. Here, we define the pulsed fraction as $M_{\mathrm{gau}}/(M_{\mathrm{gau}}+C)$, where M_{gau} is the maximum of the wider Gaussian and *C* the constant in the model. We considered the best simulated light curve model in order to exclude the *XMM-Newton* frame time binning distortion. The pulsed fraction of J1813 in the 0.3–10 keV energy range is $96\% \pm 3\%$. We note that the remaining percentage represents the maximum allowed count rate of a possible nebula. No statistically significant variations of the pulsed fraction are measured by using different energy ranges, pointing to one-component spectral models for J1813.

We performed phase-resolved spectroscopy with different selections of phase bins. In order to detect any possible spectral variation with phase, we analyzed on- and off-pulse spectra (as defined in Section 4.2), as well as the spectra of each peak. We also fitted the first and last halves of each peak. Last, we divided in three equal parts each peak. We fitted together spectra obtained from each of the described divisions of the phase. In all the cases, fixing the photon indexes we found acceptable spectral fits. An *F* test shows a non-negligible probability for a chance improvement by freeing the photon index (in each case $>1.5 \times 10^{-3}$). We conclude that no spectral variation is seen in the X-ray band as a function of the pulsar phase, with a 3σ upper limit of 0.08 in the photon index variation between on- and off-pulse phases.

5. THE HARD X-RAY BAND AND SPECTRAL ENERGY DISTRIBUTION

Searching at the position of J1813 in the hard X-ray band ($\sim$100 keV), we found a hint of a detection with Integral Soft Gamma-Ray Imager (ISGRI) and the Imager on-Board the *INTEGRAL* Satellite (IBIS) (Lebrun et al. 2003). We used the automated HEAVENS online tool[14] to create a counts map, sensitivity map, and light curve of the source with all the public *INTEGRAL* observations. The possible steady source has a count rate of 0.12 ± 0.02 counts s^{-1} in the 30–520 keV energy band, which corresponds to a flux of $\sim$5.3 $\times$ 10^{-11} erg cm^{-2} s^{-1}. Although the significance of the detection is $>6\sigma$, such a source comes from an automated script instead of from a dedicated analysis. We therefore conservatively decided to treat it as an upper limit.

In order to find the spectral energy distribution (SED) points in the X-ray band, we regrouped the *XMM-Newton* and *Chandra* spectra. We plotted the X-ray unfolded spectrum with XSPEC by using the best fitted spectral model reported in Section 4.1. To find the SED points in the γ-ray band, we divided our data set in logarithmically uniform energy bins. Then, for each bin we re-ran the binned analysis reported in Section 3. We derived the 1σ confidence *N*-dimensional ellipsoids (where *N* is the number

---

[14] http://www.isdc.unige.ch/heavens/
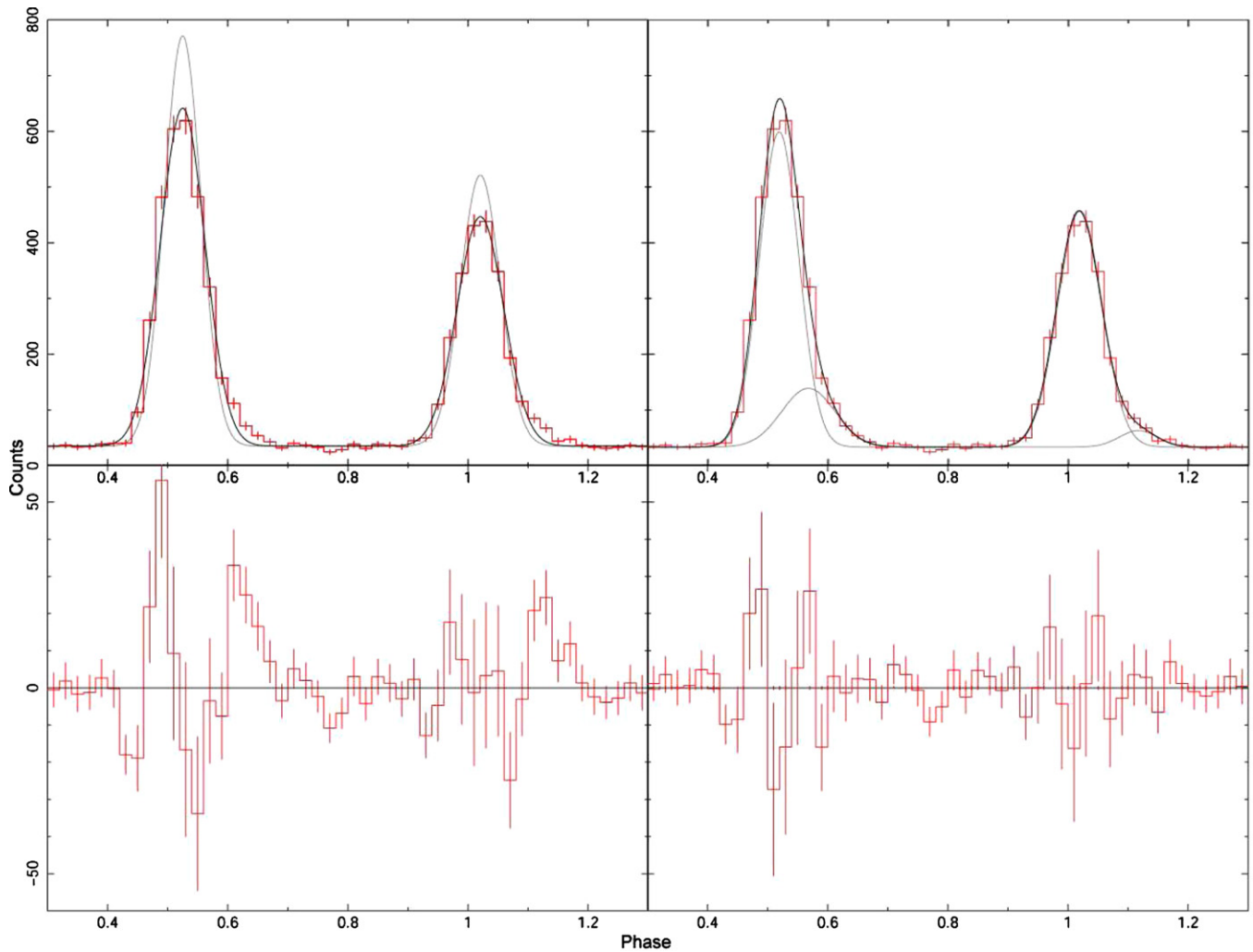
Figure 6. 0.3—10 keV weighted, nonrandomized light curve of J1813 is shown in red. Upper left: model of the X-ray light curve before the distortion due to the *XMM-Newton* frame time (gray) and after the simulation (black), which is also the best fit of the light curve by using two Gaussians and a constant. Lower left: residuals. Upper right: best fit of the X-ray light curve (black) using four Gaussians and a constant; in gray the single Gaussians components are shown. Lower right: residuals.

(A color version of this figure is available in the online journal.)

of free parameters in the models) from the covariance matrices obtained as an output of XSPEC and `gtlike` for the X-ray and γ-ray bands, respectively. Then, we simulated 10^4 spectra for each band with parameters following the contours and reported these in Figure 8 (butterfly plot). The meaning of the butterfly can be understood as follows: any absorbed power-law model (for X-rays) or power law with an exponential cutoff (for γ-rays) that is drawn on the plot which is not fully contained in the envelope is outside the 1σ confidence region for such models, and hence is excluded by the data at the 1σ confidence level.

Figure 8 clearly shows the presence of a maximum in the SED in the hard-X-ray domain—$\sim$30–500 keV. In that band, a change in the photon index—sudden or gradual—is apparent.

6. DISCUSSION

Although the observed γ-ray light curve and spectrum of J1813 are quite typical of γ-ray pulsars, the X-ray light curve and spectrum are very atypical. In other *Fermi*-LAT pulsars with nonthermal X-ray emission, like the Crab or the millisecond pulsar J1939+2134, the X-ray peaks are in phase or nearly in phase with the γ-ray peaks. This is expected in high-altitude

emission models such as the outer gap (Takata & Chang 2007) or slot gap (Harding et al. 2008), where particle acceleration and emission along the last open trailing field lines up to close to the light cylinder produces all outgoing photons at the same phase for an inertial observer (Romani & Yadigaroglu 1995; Dyks et al. 2004). Such caustic emission will produce the nonthermal γ-ray, X-ray, and optical pulses at the same phase in the light curve. In the outer gap model, the two nonthermal peaks come from the same pole, but at very different altitudes. In the slot gap model, the two nonthermal peaks come from trailing field lines from opposite poles, with the emission along leading edge field lines producing lower level off-peak emission. The fact that the observed non-thermal X-ray peaks in J1813 are not only in phase with the γ-ray peaks, but are both out of phase by about one-quarter of a period is totally unexpected and not in agreement with both X-ray and γ-ray emission being outgoing caustic emission from the outer magnetosphere.

Estimates of the emission geometry of J1813 have been obtained from fitting its light curve with a version of the outer gap and slot gap models (Pierbattista et al. 2012, 2014). These fits give an inclination angle $\alpha = 40°$ and observer angle to the spin axis $\zeta = 87°$ for the slot gap, and $\alpha = 8°$ and $\zeta = 78°$
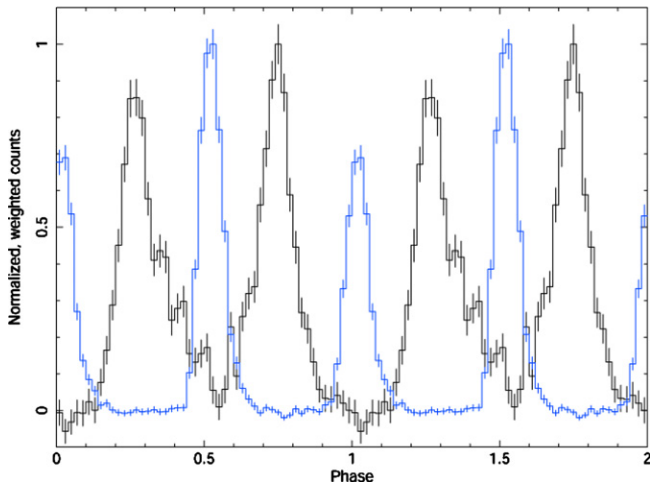
Figure 7. Phased >0.1 GeV *Fermi* light curve (black) and 0.3–10 keV *XMM-Newton* light curve of J1813 (cyan), in phase. 1σ errors are reported. The normalization is defined as in Figure 1.

(A color version of this figure is available in the online journal.)

for the outer gap model. As expected, our viewing angle is large and nearly orthogonal to the spin axis. However, the inclination angles are at least $40°$ different from the observer angle, as expected for a radio-quiet pulsar, given that a small $\beta = \alpha - \zeta$ is required in order to miss the radio beam along the magnetic pole. The slot gap is slightly favored over the outer gap in the fit, but not significantly so.

In many outer magnetosphere emission models, such as the outer gap and the slot gap, the nonthermal optical to X-ray emission is synchrotron radiation from electron–positron pairs. In the outer gap models, pairs are accelerated and radiate in both outward and inward directions, so it might be possible to see a synchrotron component from ingoing electrons or positrons. However, it is then not clear why the outgoing radiation is also not visible. In slot gap models, all emission is assumed to be outgoing since the primary particles are only accelerated outward and the electron–positron pairs from polar cap cascades, which radiated the nonthermal synchrotron emission, are also only outgoing. However, from simulations of global magnetospheres (see, e.g., Spitkovsky 2006; Timokhin 2006), currents appear in both directions since there must be a return current. The actual composition of these currents is not presently known (the models only give the macroscopic current density), but it is possible that the main current consists of electrons flowing outward and the return current of electrons flowing inward. Recent dissipative pulsar magnetosphere models (Kalapotharakos et al. 2012; Li et al. 2012) derive the electric field parallel to the magnetic field ($E_\parallel$) as well as the (macroscopic) currents and charge densities. The $E_\parallel$ components appear in both directions, on different field lines, so, depending on the sign of charge that is present along each field line, charges could be accelerated and radiate inward on some field lines (or even in both directions).

We have tested the possibility that the X-ray emission in J1813 is not outgoing but ingoing radiation. In this case, geometrically, ingoing emission from leading file lines may produce caustics that would be out of phase with the outgoing caustic from trailing edge field lines. We simulated ingoing emission radiated tangent to field lines using a geometric representation of the slot gap, known as two-pole caustic geometry (Dyks & Rudak 2003). Uniform emissivity was assumed, along the field lines with footprints lying between $r_{ovc} = 0.95$ and $r_{ovc} = 1.0$, where r_{ovc} are open volume radius coordinates on the polar cap (see, e.g.,

Dyks et al. 2004), where $r_{ovc} = 0.0$ is the magnetic axis and $r_{ovc} = 1.0$ is the outer rim of the polar cap. The ingoing emission was traced from an outer radius of $r_{max} = 1.2$, in units of light cylinder radius, $R_{LC} = c/\Omega$, to the neutron star surface, in both vacuum retarded dipole (Dyks & Harding 2004) and force-free (Contopoulos & Kalapotharakos 2010; Harding et al. 2011) magnetic fields. We find that the resulting emission pattern in observer angle versus phase with respect to the rotation axis does indeed show caustics, but the peaks in the light curves do not have phase offsets with the outgoing emission peaks that are near 0.25.

We then explored the possibility that the γ-ray emission comes from the outer magnetosphere and the X-ray emission comes from the pair cascades above the polar caps. We simulated the γ-ray emission in a force-free magnetosphere, using a geometry for outgoing emission similar to that of the separatrix model (Bai & Spitkovsky 2010) between $r_{ovc} = 0.95$ and $r_{ovc} = 0.99$. The maximum emission radius was assumed to be $r_{max} = 1.5$, with a maximum cylindrical radius of $r_h = 2.0$, so that some emission comes from outside the light cylinder, near the current sheet. The photon emission directions are entirely determined in the nonrotating inertial frame, as in Bai & Spitkovsky (2010), where the photons are emitted parallel to the particle velocity which is a sum of the drift velocity and a component parallel to the local magnetic field line. A sky map of the emission in observer angle ζ versus phase ϕ with respect to the rotation axis for a magnetic inclination angle $\alpha = 60°$ is shown in Figure 9 (see Bai & Spitkovsky (2010) Figure 9). In this map, the magnetic poles are located at $\phi = 0$, $\zeta = 120°$, $\phi = 0.5$, $\zeta = 60°$. An observer at $\zeta = 90°$ (white horizontal line) will cut through the caustic pattern twice to see two peaks at $\phi \sim 0.16$ and $\phi \sim 0.67$, as shown in Figure 9.

We simulated the X-ray emission as a cone beam with peak emission just inside the polar cap rim $r_{ovc} = 1.0$. Since the cone beam function modulates the emission along all field lines, we allow emission between $r_{ovc} = 0.1$ and $r_{ovc} = 1.2$. The cone beam geometry is the same as described in Story et al. (2007), but we allow the altitude of the emission to be a free parameter at a given radius, which was adjusted to supply a negative phase shift. This phase shift, when added to the positive phase shift of the γ-ray peaks, can supply the total phase offset between γ-ray and X-ray peaks. We find that an X-ray emission altitude of around $r = 0.2R_{LC}$ is needed to give a total phase shift near the observed value. A sky map of the simulated cone emission for this case is shown in Figure 9 for an inclination angle $\alpha = 60°$. An observer at $\zeta = 90°$ (white horizontal line) will cut through cones from both magnetic poles to see two peaks in the light curve. As shown in Figure 9, the phase offset between the X-ray and γ-rays peaks is around 0.24, so this scenario seems promising. However, the radio cone beam emission would occur at a lower altitude, forming a smaller cone in the sky map to avoid detection. If retarded vacuum dipole field geometry is used instead to simulate the γ-ray light curve, the first γ-ray peak would lie at phase ~ 0.08, and the X-ray cone beam would need to be at an implausibly high altitude to make up a total phase offset near 0.25. The force-free field geometry is therefore strongly favored in this scenario.

We note that such a model is in agreement with the empirical results from Marelli et al. (2011): as reported, an important difference in both the positions and heights of the X-ray and γ-ray emitting regions would fully explain the large spread of the distance-independent X-ray-to-γ-ray flux ratio they found. Moreover, as reported in Marelli et al. (2014),
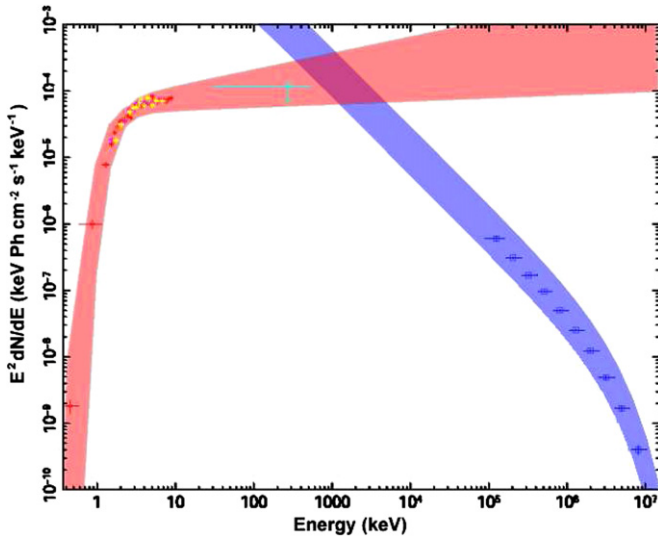
Figure 8. Spectral energy distribution of J1813. Red, magenta, orange, and yellow star points mark the unfolded 0.4–10 keV spectra from *XMM-Newton* PN, MOS1, MOS2, and *Chandra*, respectively. Blue square points result from binned likelihood spectral analysis of *Fermi* data of logarithmically uniform energy bins. The cyan round point reports the hint of detection with *INTEGRAL* IBIS/ISGRI, which we conservatively chose to treat as an upper limit. The red area is the X-ray 1σ butterfly for the absorbed model: any X-ray-band absorbed power-law model that is drawn on the plot which is not fully contained in the envelope is excluded by the data at the 1σ confidence level. Similarly, the blue region is the γ-ray 1σ butterfly, using a power law with exponential cutoff. We note that these regions are verified only in the X-ray (0.3–10 keV) and γ-ray (0.1–100 GeV) band and then extrapolated to the full plot.

the alignment between thermal and nonthermal X-ray peaks noted for many pulsars (see, e.g., Geminga, PSR J0659+1414, PSR J1057−5226, and PSR J1741−2054; De Luca et al. 2005; Marelli et al. 2014) further suggests that the nonthermal emission is generated in a region near the pulsar poles (e.g., in our polar cap emission model). Also, the low X-ray luminosity of radio-quiet pulsars in the X-ray band (Marelli et al. 2011) suggests that the radio and X-ray emission regions may be in close proximity. A future, deeper exploration of these pulsar emission characteristics, together with the modeling of each pulsar, will be able to confirm or rule out our X-ray polar-cap emission model.

The very hard X-ray spectrum (as a comparison, the Crab has a photon index of 1.6 and Vela of 2.7) and relatively high X-ray flux of J1813 are also unusual for its age. In the γ-ray-emitting pulsar zoo, only PSR J1811−1926, and possibly J2229+6114, have a similar hard spectrum (Marelli et al. 2011). We note that the three pulsars are quite similar in period, age, and energetics. Moreover, we did not detect any thermal emission from this pulsar. Very young pulsars, like the Crab and B1509−58, have high levels of nonthermal X-ray flux relative to γ-ray flux, and no detected thermal emission. Middle-aged pulsars, such as Vela and B0656+14, have dominant thermal emission that is best fit with hot and cool components, plus a smaller power-law component. Given that one expects the presence of both heating and cooling thermal emission in a pulsar of this age (43 kyr), the relative level of the nonthermal emission is much higher than seen for other middle-aged pulsars. An estimate of the expected thermal component in J1813 from polar cap heating from Harding & Muslimov (2001) is $L_{PC} = 3 \times 10^{31}$ erg s^{-1} from a surface with a ∼400 m radius (De Luca et al. 2005). From Pons et al. (2009), we can also expect a thermal cooling component from the entire surface $L_{\rm cool} \gtrsim 7 \times 10^{31}$ erg s^{-1}.
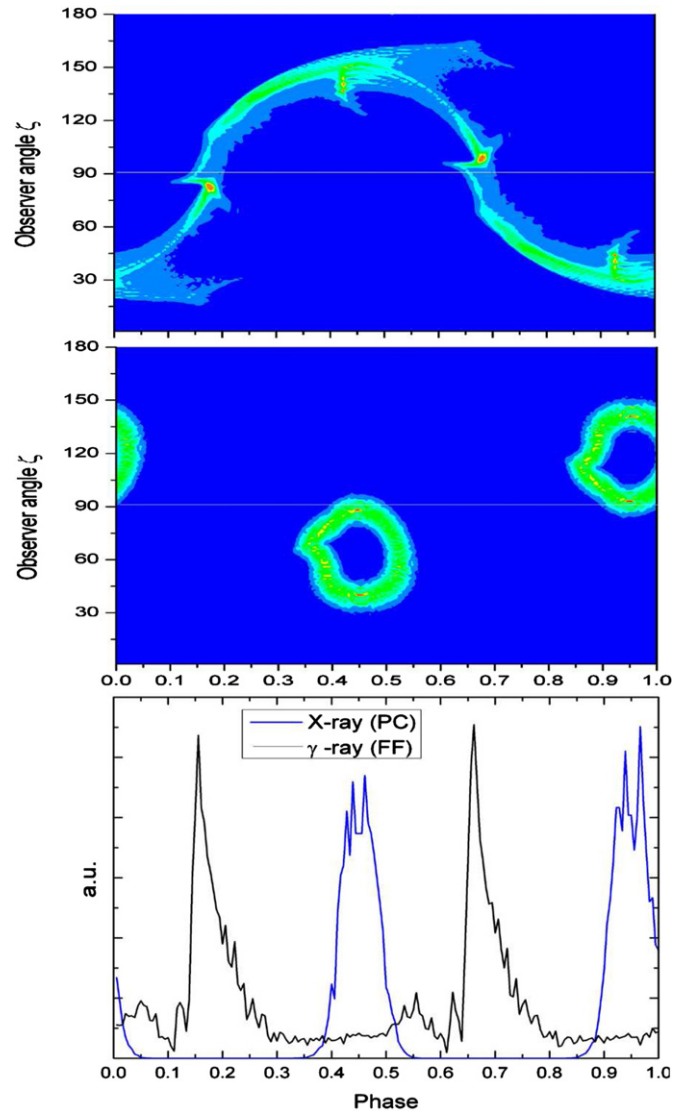
Figure 9. Sky maps of emission in observer angle ζ vs. phase φ with respect to the rotation axis for a magnetic inclination angle $\alpha = 60°$ for (a) simulated γ-ray caustic emission from the outer magnetosphere for a separatrix layer model in a force-free magnetic field, and (b) simulated cone beam X-ray emission from the polar caps for an emission altitude $r = 0.2R_{rmLC}$. (c) Model γ-ray (black) and X-ray (blue) light curves for a viewing angle of $\zeta = 90°$ (white lines in the sky maps).

Under the hypothesis of a pulsar distance of 2.5 kpc, neither component would be detected due to the high absorption. We can set upper limits for the polar cap heating luminosity at $L_{PC} \lesssim 5.6 \times 10^{31}$ erg s^{-1} and thermal cooling luminosity at $L_{\rm cool} \lesssim 1.3 \times 10^{33}$ erg s^{-1}. We conclude that the lack of detection of thermal emission from J1813 is due to the high absorption.

The non-thermal X-ray flux of J1813 is relatively high compared to its γ-ray flux. In fact, its γ-ray-to-X-ray flux ratio is 234 ± 6, three times less than the lowest one of the radio-quiet pulsar family (Marelli et al. 2011; Abdo et al. 2013). We question whether J1813 is a radio-quiet pulsar or a radio-loud one with its radio counterpart unobservable due to the large distance. Its upper limit radio flux at 1400 MHz is 17 μJy (Ray et al. 2011). J1813 falls just below the value of 30 μJy conventionally used to divide radio-quiet and radio-loud pulsars (Abdo et al. 2013), but over the threshold in pseudo-luminosity of 100 μJy kpc^2 for distances ≳2.5 kpc. For comparison, J0106+4855 and J1907+0602 are at a distance of ∼3 kpc and

have radio fluxes of 8 and 3.4 μJy, respectively, with γ-ray-to-X-ray flux ratios compatible with those of radio-loud pulsar family. On an observational basis, we therefore cannot conclude that J1813 does not emit in the radio band. We nevertheless stress that emission geometry estimates by Pierbattista et al. (2012) point to a lack of radio emission along our line of sight.

From J1813 X-ray (0.3–10 keV) off-pulse spectroscopy, we can derive a 3σ flux upper limit for a possible nebula of 1.5×10^{-13} erg cm^{-2} s^{-1}, with a photon index of 1.25 ± 0.21 (1σ error). A photon index higher than that of the pulsar is in agreement with theoretical expectations for synchrotron-emitting nebulae. Such a value corresponds to a 100% pulsed fraction from the pulsar, so that all the off-pulse emission comes from the nebula. Kargaltsev & Pavlov (2008) correlate the nebular and nonthermal pulsar X-ray luminosities for all the nebulae detected by *Chandra*. Our upper limit nebular flux is barely in agreement with the lower bound of their relation. This would require that most of the unpulsed component of our source comes from the nebula, making the pulsar about 100% pulsed. From the analysis of the *Chandra* PSF, the nebula must be within a 1″.5 radius of the pulsar. Assuming standard relations (Gaensler & Slane 2006), the distance between the pulsar and the head of the termination shock is expected to be $r_s = (\dot{E}/4\pi c \rho_{ISM} v_{psr}^2)^{1/2}$, where ρ_{ISM} is the ambient density and v_{psr} is the pulsar space velocity. For a typical pulsar velocity (500 km s^{-1}) and ambient density (0.1 atoms cm^{-3}) at 2.5 kpc, this would place the shock at 5″ from the pulsar (for instance, Vela nebula would have a 5″ radius at 2.5 kpc). In any case, we see no sign of a nebula down to 1″.5: this requires a very high pulsar velocity ($>$1800 km s^{-1}) and/or interstellar medium density ($>$1.3 cm^{-3}) and/or pulsar distance ($>$9 kpc).

From the J1813 SED, we can argue that there is a discontinuity (smooth or sudden) in the photon index in the hard X-ray band. The youngest pulsars (Crab, PSR B1509−58) usually have similar SEDs, peaked in hard X-rays, and with a smooth connection between γ-rays and X-rays (Kaspi et al. 2006). We suggest that J1813 could be younger than its characteristic age ($\tau_c = 43$ kyr). Nevertheless, we note that while the X-ray thermal emission from a 5–10 kyr old supernova nemnant (SNR) would not be detected due to the high absorption column, we would expect a pulsar wind nebula brighter than usual from the interaction of the pulsar and the SNR (see, e.g., Bucciantini et al. 2011). Middle-aged pulsars instead have comparatively weak, nonthermal emission in the X-ray band since their power peaks at GeV energies, and there is a gap in the detected spectrum between the X-ray and γ-ray bands. In several cases (Vela, PSR B1055−52), an extrapolation between the two is plausible, but in others (Geminga, PSR B1706−44; Gotthelf et al. 2002) a connection is not clear. In order to discriminate different multi-wavelength emission models, the spectrum and timing of J1813 in the hard X-ray band would be of the upmost importance.

7. CONCLUSIONS

We have analyzed our recent, deep *XMM-Newton* and *Chandra* observations of the energetic radio-quiet PSR J1813−1246. We have also extended the γ-ray ephemeris to a five-year period. J1813 had two glitches during this time period. Its γ-ray light curve is characterized by two peaks, separated by 0.5 in phase, with a bridge in between. No off-pulse emission has been detected. A phase-resolved spectral analysis revealed a change in the photon index, with a softening during the peaks. The X-ray spectrum is nonthermal, harder than all the other

Fermi pulsars ($\Gamma = 0.85 \pm 0.03$), and highly absorbed ($N_H = 1.56 \pm 0.07 \times 10^{22}$ cm^{-2}). Detection of thermal emission (from hot spots and from cooling) was not expected due to the high absorption column. Based on such absorption, on the analysis of serendipitous sources around the pulsar and on radio observations of the numerous dark clouds in the J1813 region, we propose that J1813 is more than 2.5 kpc distant. Such a large distance would make faint radio pulsations undetectable, even if geometrical models point toward a radio-quiet pulsar. We also found a hint of detection in the *INTEGRAL* IBIS/ISGRI band (30–500 keV) that perfectly matches the spectral energy distribution of J1813. We detected X-ray pulsations with very high confidence, with a light curve characterized by two sharp, asymmetrical peaks, separated by 0.5 in phase. Differently from all the other known pulsars, the X-ray peaks lag behind the γ-ray ones by a quarter of phase. The pulsed fraction of the X-ray source is 96 ± 3%, with a faint off-pulse emission detected that can be due to nebular emission, which is nevertheless undetectable through brightness profile analysis down to 1–1″.5. A phase-resolved spectral analysis revealed no significant X-ray spectral changes during the pulsar phase.

Outer gap and slot gap models predict shapes similar to our γ-ray profile for very high observer angles to the spin axis (87° and 78°, respectively). In high-altitude emission models, particle acceleration and emission along the last open trailing field lines up to near the light cylinder is expected to produce nonthermal γ-ray, X-ray, and optical pulses at the same phase in the light curve. The fact that the observed nonthermal X-ray peaks in J1813 are not only not in phase with the γ-ray peaks, but are both out of phase by about one-quarter of a period, is not in agreement with both X-ray and γ-ray emission being outgoing emission from the outer magnetosphere. It is possible that the γ-ray emission comes from the outer magnetosphere and the X-ray emission comes from the polar cap, but at an altitude of about 40 neutron star radii. The phase offset between γ-ray and X-ray peaks requires the use of force-free magnetic field geometry in modeling the light curves. X-ray emission from polar cap pair cascades is mostly synchrotron radiation from secondary electron–positron pairs that are produced with a broad spectrum of energies (Daugherty & Harding 1982). The emission can extend from a few tenths of a keV up to 10–100 MeV (Dyks & Rudak 1999), so could plausibly explain the spectrum of J1813. If this is the case, it would be the first time that a clear emission from the polar cap pair cascades has been observed.

Table 2
Analysis of Serendipitous Sources

Source	J2000 Coord	N_H	Spectrum	HR	$\log(\frac{f_X}{f_V})$
. . .	. . .	$(10^{22} \, \text{cm}^{-2})$	. . .	. . .	. . .
3	273.5839−12.7397[a]	$0.91 \pm 0.15/0.88 \pm 0.14$	?	?	−0.69
4	273.2630−12.8186[b]	2.1 ± 0.4	AGN	AGN	$m_R > 25.4$[d]
5	273.2210−12.6814[a]	1.7 ± 0.3	AGN	AGN	$m_R > 23.9$[d]
6	273.3608−12.8407[b]	$0.40 \pm 0.08/0.98 \pm 0.20$	?	star	−1.93/−2.32/−0.94
7	273.3553−12.7529[b]	0.81 ± 0.15	star	star	−2.50[c]
8	273.3029−12.6696[a]	1.7 ± 0.6	AGN	AGN	$m_R > 24.9$[d]
9	273.5829−12.7871[a]	$0.44 \pm 0.18/0.33 \pm 0.16$	?	?	−1.62[c]
10	273.4600−12.7828[a]	1.1 ± 0.6	AGN	AGN	$m_R > 22.9$[d]
11	273.4489−12.7895[a]	0.84 ± 0.13	star	star	−3.43[c]

Notes. Results of the serendipitous sources analysis. Here we report the best X-ray position, the classification following the spectral and HR methods described in Section 7 and the logarithm of the X-to-optical flux ratio (for all the possible optical counterparts). We also report the best fitted column density of the source; if the spectrum is well fitted both by power law and apecs, we report both the values, respectively. The X-ray flux is unabsorbed and in the 0.3–10 keV energy range. The optical flux is unabsorbed and in the *V* band from the NOMAD catalog. The errors on column densities are at a 90% confidence.
[a] Position obtained by *XMM-Newton*; typical 90% error box of 5″.
[b] Position obtained by *Chandra*; typical 90% error box of 2″.
[c] For these sources, a proper motion has been detected and reported in the NOMAD catalog.
[d] For the high fitted absorption column of AGN-like sources, we reported the expected observable magnitude, based on La Palombara et al. (2006). Such counterparts are not detectable in the NOMAD catalog.

APPENDIX

Based on the study of spectra and possible optical counterparts, we can classify serendipitous sources as AGNs or candidate stars, allowing us to constrain the pulsar distance. Indeed, after selecting candidate AGNs in the FOV, it is possible to measure from their spectra the total Galactic column density in the direction of J1813.

As a first step, we studied the brightness profile of each source and compared it with the theoretical (for *XMM-Newton* data) or simulated (for *Chandra* data) PSF. All the detected sources are point-like. We performed a standard *XMM-Newton* and *Chandra* spectral analysis for the nine sources detected at $>10\sigma$ and with more than 300 *XMM-Newton* net total counts. The main discriminator among different classes of X-ray-emitting objects is the spectral shape. The spectra were fitted either with an absorbed power law, well-suited for AGNs, and absorbed double apecs (emission spectrum from collisionally ionized diffuse gas), well-suited for stellar coronae. From studies on serendipitous X-ray sources in *Chandra* and *XMM-Newton* observations (see, e.g., Novara et al. 2009; Ebisawa et al. 2002), the detection probability for other X-ray emitting source classes in our mid-Galactic-latitude *XMM-Newton* observation is negligible. Four out of the nine considered sources can be fitted only by an absorbed power law (sources #4,#5,#8,#10), prompting their AGN classification, and two only by double apecs (sources #7,#11), suggesting a stellar classification, while three remained unclassified.

Since the count statistics of some of the selected X-ray sources is too low to discriminate the spectral model, we performed a qualitative spectral analysis using the count rate (CR). We measured it in the three energy ranges (soft: 0.3–1 keV; medium: 1–2 keV; hard: 2–10 keV) to compute two different hardness ratios (HRs):

$$\text{HR12} = [\text{CR}(1-2) - \text{CR}(0.3-1)]/[\text{CR}(1-2) + \text{CR}(0.3-1)]$$
$$\text{HR23} = [\text{CR}(2-10) - \text{CR}(1-2)]/[\text{CR}(2-10) + \text{CR}(1-2)].$$

Adopting the above definition, sources with a small/large HR12 value are little/very absorbed, while sources with a small/large HR23 value are characterized by a soft/hard spectrum.

Figure 10 shows the distribution of the HRs of the nine serendipitous X-ray sources. To obtain a further indication on the spectra of the sources, we compared the measured HRs with the expected ones computed for two different template spectral models, namely: a power law with photon indexes Γ increasing from 1.5 to 2.5, and an apec with temperatures kT increasing from 0.5 to 5.5 keV. Each spectral model is computed using the average interstellar medium absorption given by Dickey & Lockman (1990) and three times that value (which is the highest value fitted among the serendipitous sources spectra). The values of the expected HRs are overplotted in Figure 10.

Sources #6, #7, and #11 are little absorbed and are characterized by a rather soft spectrum (HR12 < 0.5 and HR23 < 0), pointing to a (nearby) star classification. Sources #4, #5, #10, and #8 are probably situated farther than the dark cloud for their high absorption; their hard spectra suggest that they are likely AGNs. Such a method confirms the spectral results, also adding source #6 to the pool of stars.

Another common way to confirm X-ray classification of sources is based on multi-wavelength analysis: the X-ray-to-optical flux ratio is a good indicator of the nature of X-ray emitters. According to La Palombara et al. (2006), AGNs have typical logarithms of X-ray-to-optical flux ratios higher than
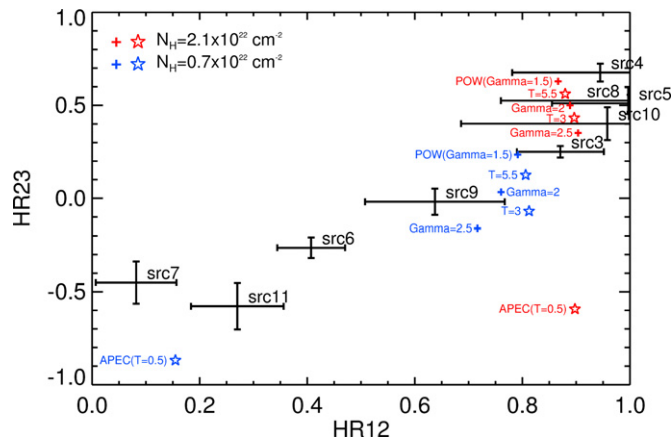
Figure 10. Distribution of HR12 vs. HR23 of the nine selected X-ray sources. Error bars are reported at 1σ. Crosses indicate the expected HR12 vs. HR23 computed for power-law spectra with Γ from 1.5 and 2.5. Stars indicate the expected HR12 vs. HR23 computed for apec spectra with kT from 0.5 to 5.5 keV. Each spectral model is computed using the average interstellar medium absorption given by Dickey & Lockman (1990) (red) and thrice that value (blue).

(A color version of this figure is available in the online journal.)

-0.2, while stars lower than $+1.0$. Inside each X-ray source error box, we looked for association with optical sources from the NOMAD catalog (Zacharias et al. 2005), considering the *V*-band magnitude as reference. When the *V*-band magnitude was not available for the candidate counterpart, we alternatively used the *R* magnitude. In the case of J1813 field, however, we do not expect to find the optical counterparts of AGNs due to the surprisingly high value of our column densities: in fact, we expect magnitudes well above the NOMAD upper limit of $m = 21$. Few of our AGN-like objects have optical counterparts inside their error box that could be due to spurious matches. In order to estimate the number of spurious matches, we used the relation from Severgnini et al. (2005) and Novara et al. (2009). This yielded a probability of chance coincidence of 21%, which means that, at our limiting magnitudes, contamination effects cannot be ignored. Each of the star-like objects has an optical counterpart that agrees with the expected X-ray-to-optical flux ratio. Table 2 reports the associated optical counterparts and expected upper limits for AGNs.

Thus, we identified four out of the nine sources we considered as AGNs and three of them as stars. The remaining two objects have possible star-like optical counterparts which yield reasonable X-ray-to-optical flux ratios. The faintness of the optical counterparts precludes any further analysis.

REFERENCES

Abdo, A. A., Ackermann, M, Ajello, M., et al. 2009a, Sci, 325, 840
Abdo, A. A., Ackermann, M, Ajello, M., et al. 2009b, ApJS, 183, 46
Abdo, A. A., Ajello, M., Allafort, A., et al. 2013, ApJS, 208, 17
Abergel, A., Ade, P. A. R., Aghanim, N., et al. 2014, arXiv:1312.1300
Bai, X.-N., & Spitkovsky, A. 2010, ApJ, 715, 1282
Bevington, P. R. 1969, Data Reduction and Error Analysis for the Physical Sciences (New York: McGraw-Hill)
Buccinantini, N., Arons, J, & Amato, E. 2011, MNRAS, 410, 381
Caraveo, P. A. 2014, ARA&A, 52, 211
Caraveo, P. A., De Luca, A., Mereghetti, S., Pellizzoni, A., & Bignami, G. F. 2004, Sci, 305, 376
Cash, W. 1979, ApJ, 228, 939
Contopoulos, I., & Kalapotharakos, C. 2010, MNRAS, 404, 767
Cheng, K. S., Ho, C., & Ruderman, M. 1986, ApJ, 300, 500
Dame, T. M., Hartmann, D., & Thaddeus, P. 2001, ApJ, 547, 792

Daugherty, J. K., & Harding, A. K. 1982, ApJ, 252, 337
De Jager, O., & Busching, I. 2010, A&A, 517, 9
De Luca, A., Caraveo, P. A., Mereghetti, S., Negroni, M., & Bignami, G. F. 2005, ApJ, 623, 1051
Dickey, J. M., & Lockman, F. J. 1990, ARA&A, 28, 215
Dobashi, K. 2011, PASJ, 63, 1
Dyks, J., & Harding, A. K. 2004, ApJ, 614, 869
Dyks, J., Harding, A. K., & Rudak, B. 2004, ApJ, 606, 1125
Dyks, J., & Rudak, B. 1999, MNRAS, 303, 477
Dyks, J., & Rudak, B. 2003, ApJ, 598, 1201
Ebisawa, K., Paizis, A., Maeda, Y., et al. 2002, Black Hole Astrophysics, 6th Proc. APCTP Winter School, Held 2002 January 9–12 in Pohang, Korea, ed. H. K. Lee & M.-G. Park (Singapore: World Scientific Publishing), 25
Gaensler, B. M., & Slane, P. O. 2006, ARA&A, 44, 17
Garmire, G. G., Bautz, M. W., Ford, P. G., et al. 2003, Proc. SPIE, 4851, 28
Gotthelf, E. V., Halpern, J. P., & Dodson, R. 2002, ApJ, 567, 125
Harding, A. K. 2013, JASS, 30, 145
Harding, A. K., DeCesar, M. E., Miller, M. C., Kalapotharakos, C., & Contopoulos, I. 2011, arXiv:1111.0828
Harding, A. K., & Muslimov, A. G. 2001, ApJ, 556, 987
Harding, A. K., & Muslimov, A. G. 2004, 35th COSPAR Scientific Assembly, 35, 562
Harding, A. K., Stern, J. V., Dyks, J., & Frackowiak, M. 2008, ApJ, 680, 1378
Hou, L. G., Han, J. L., & Shi, W. B. 2009, A&A, 499, 473
Kalapotharakos, C., Harding, A. K., Kazanas, D., & Contopoulos, I. 2012, ApJ, 754, 1
Kalberla, Burton, P. M., W. B., & Hartmann, D. 2005, A&A, 440, 775
Kargaltsev, O., & Pavlov, G. G. 2008, in AIP Conf. 983, 40 YEARS OF PULSARS: Millisecond Pulsars, Magnetars and More, ed. C. G. Bassa, Z. Wang, A. Cumming, & V. M. Kaspi (Melville, NY: AIP), 171
Kaspi, V. M., Roberts, M. S. E., & Harding, A. K. 2006, in Compact Stellar X-ray Sources, ed. W. Lewin & M. van der Klis (Cambridge Astrophysics Series, No. 39; Cambridge: Cambridge Univ. Press), 279
Kerr, M. 2011, ApJ, 732, 38
Kuntz, K. D., & Snowden, S. L. 2008, A&A, 478, 575
Kuster, M., Benlloch, S., Kendziorra, E., & Briel, U. G. 1999, Proc. SPIE, 3765, 673
La Palombara, N., Mignani, R. P., Hatziminaoglou, E., et al. 2006, A&A, 458, 245
Lebrun, F., Leray, J. P., Lavocat, P., et al. 2003, A&A, 411, 141
Li, J., Spitkovsky, A., & Tchekhovskoy, A. 2012, ApJ, 746, 60
Marelli, M., De Luca, A., & Caraveo, P. A. 2011, ApJ, 733, 82
Marelli, M., Belfiore, A., Saz Parkinson, P., et al. 2014, ApJ, 790, 51
Marelli, M., De Luca, A., Salvetti, D., et al. 2013, ApJ, 765, 36
Mattox, J. R., Bertsch, D. L., Chiang, J., et al. 1996, ApJ, 461, 396
McClure-Griffiths, N. M., Pisano, D. J., Calabretta, M. R., et al. 2009, ApJS, 181, 398
Mitsuda, K., Bautz, M., & Inoue, H. 2007, PASJ, 59, 1
Nolan, P. L., Abdo, A. A., Ackermann, M., et al. 2012, ApJS, 199, 31
Novara, G., La Palombara, N., Mignani, R. P., et al. 2009, A&A, 501, 103
Pierbattista, M. Grenier, I. A., Harding, A. K., & Gonthier, P. L. 2012, A&A, 545, 42
Pierbattista, M., Harding, A. K., & Grenier, I. A. 2014, A&A, submitted (arXiv:1403.3849)
Pons, J. A., Miralles, J. A., & Geppert, U. 2009, A&A, 496, 207
Protassov, R., Van Dyk, D. A., Connors, A., Kashyap, V. L., & Siemiginowska, A. 2002, ApJ, 571, 545
Ray, P. S., Kerr, M., Parent, D., et al. 2011, ApJS, 194, 17
Read, A. M. 2004, XMM-CCF-REL-167
Romani, R. W., & Yadigaroglu, I. A. 1995, ApJ, 438, 314
Saz Parkinson, P. M., Dormody, M., Ziegler, M., et al. 2010, ApJ, 725, 571
Severgnini, P., Della Ceca, R., Braito, V., et al. 2005, A&A, 431, 87
Skrutskie, M. F., Cutri, R. M., Stiening, R., et al. 2006, AJ, 131, 1163
Spitkovsky, A. 2006, ApJ, 648, 51
Story, S. A., Gonthier, P. L., & Harding, A. K. 2007, ApJ, 671, 713
Struder, L., Briel, U., Dennerl, K., et al. 2001, A&A, 365, L18
Takata, J., & Chang, H. K. 2007, ApJ, 670, 677
Timokhin, A. N. 2006, MNRAS, 368, 1055
Treves, A., Popov, S. B., Colpi, M., Prokhorov, M. E., & Turolla, R. 2001, in ASP Conf. Ser. 234, X-ray Astronomy, ed. R. Giacconi, S. Serio, & L. Stella (San Francisco, CA: ASP), 225
Turner, M. J. L., Abbey, A., Arnaud, M., et al. 2001, A&A, 365, 27
Wang, Z., Breton, R. P., Heinke, C. O., Deloye, C. J., & Zhong, J. 2013, ApJ, 765, 151
Watters, K. P., & Romani, R. W. 2011, ApJ, 727, 123
Zacharias, N., Monet, D. G., Levine, S. E., et al. 2005, yCat, 1297, 0